buildings

MDPI

Article

Wind-Induced Vibration Characteristics and Shading Effects of a Double-Layer Cable-Supported Photovoltaic Module System Based on Wind Tunnel Test

Zhenkai Zhang [1,2,*], Zhiyu Xiao [1], Wenyong Ma [1,3] and Xinyue Liu [1]

[1] School of Civil Engineering, Shijiazhuang Tiedao University, 17 North Second Ring East Road, Shijiazhuang 050043, China; xzy18531908818@163.com (Z.X.); ma@stdu.edu.cn (W.M.); liuxinyue4468@163.com (X.L.)
[2] Key Laboratory of Roads and Railway Engineering Safety Control, Shijiazhuang Tiedao University, 17 North Second Ring East Road, Shijiazhuang 050043, China
[3] Innovation Center of Wind Engineering & Wind Energy Technology Hebei, Shijiazhuang Tiedao University, 17 North Second Ring East Road, Shijiazhuang 050043, China
* Correspondence: heutzhangzhenkai@163.com

Abstract: The double-layer (DL) cable-supported photovoltaic (PV) module system is an emerging type of structure that has garnered significant attention in recent years due to its large span, strong terrain adaptability, and economic advantages. As it is a flexible structure supported by cables, wind-induced vibrations can lead to structural instability or even component damage, posing a serious threat to the safety of PV power plants. Determining the wind-induced vibration characteristics of the DL cable-supported PV module system is the foundation for ensuring its structural safety. In this study, based on wind tunnel tests performed on an aeroelastic model, a typical DL cable-supported PV module system used in a real engineering project was examined. The wind-induced displacement and torsional vibration characteristics of the model were compared and analyzed under different wind speeds. The shading effects of the PV array were also studied, and the impact of different wind angles and the initial tilt angles of PV modules on the wind-induced vibration characteristics was revealed. The results show that the greatest displacement vibration response occurs in the vertical direction; in comparison, displacements in other directions are smaller. Wind-induced torsional vibrations are negligible and can be ignored compared to displacement vibrations. The wind-induced vibration of the first row in the cable-supported PV array is significantly greater than that of the subsequent rows, and the shading effect is obvious. In the same row, the displacement vibration of modules at the center span is greater than at the sides. Different wind angles and initial PV module tilt angles affect the wind-induced vibration characteristics. When the wind direction is perpendicular to the cables and wind suction occurs, the wind-induced vibration is maximal. Within a limited range, the larger the initial tilt angle of the PV module, the greater the wind-induced vibration.

Keywords: DL cable-supported PV module system; wind-induced vibration characteristics; shading effects; wind tunnel test

Academic Editors: Xiaodi Dai and Luchuan Ding

Received: 13 January 2025
Revised: 29 January 2025
Accepted: 6 February 2025
Published: 11 February 2025

Citation: Zhang, Z.; Xiao, Z.; Ma, W.; Liu, X. Wind-Induced Vibration Characteristics and Shading Effects of a Double-Layer Cable-Supported Photovoltaic Module System Based on Wind Tunnel Test. *Buildings* **2025**, *15*, 550. https://doi.org/10.3390/buildings15040550

1. Introduction

Faced with the global climate crisis and the increasing demand for clean energy, replacing fossil fuels with renewable energy sources has become an ideal solution. Among the available renewable energy sources, solar energy has become one of the most favored

options due to its clean, safe, and inexhaustible nature. Photovoltaic (PV) module systems, including the supporting structures and PV modules, are critical for the effective operation and economic viability of PV power plants. The design of these supports directly impacts both the performance and the investment costs of PV power stations. Researchers have proposed various types of PV support structure to meet the diverse construction needs of PV power stations in different environments such as rooftops, deserts, tidal flats, and farms. Wind-induced damage is the most significant threat to the structural safety of PV module systems. Based on different wind-induced vibration characteristics, existing PV module systems can be categorized into fixed PV systems, tracking PV systems, and flexible PV module systems.

Fixed PV module systems generally comprise steels fixed together, and the tilt angle of the PV modules does not change with the incident angle of sunlight. These types of system are safe and reliable, with them typically not exhibiting noticeable wind-induced vibrations. Research on fixed PV module systems began as early as the 1980s [1], primarily focusing on wind load coefficients and the impact of various factors on wind loads. Fixed PV supports can be further categorized into ground-mounted and rooftop-mounted systems. For ground-mounted systems, researchers have analyzed the effects of building width, side ratio, length-to-width ratio, roof slope, and parapet walls on the wind loads on PV supports [2–6]. For rooftop-mounted systems, researchers have analyzed the impact of row spacing, tilt angle, and shading effects on wind load values [7–18]. Research on fixed PV supports is relatively mature, and integrated optimization designs considering both the mechanical performance of PV modules and the structural performance of supports are expected to constitute future research directions.

Fixed PV supports are highly safe and cost-effective, however, it is not possible to adjust the tilt angle of the PV modules according to the sun's incident angle, leading to lower energy utilization. To address this issue, researchers have developed solar-tracker PV supports [19,20]. Such tracking systems allow the PV modules to track the incident angle of the sun, effectively improving energy utilization. However, solar-tracker PV supports have lower torsional stiffness and, under wind loads, may exhibit significant aerodynamic coupling effects, leading to large torsional vibrations and damage [21]. Most studies on solar-tracker PV supports have focused on the determination of wind loads and the analysis of wind-induced vibration characteristics. For instance, wind tunnel tests and numerical simulations have been used to analyze wind load values and the interference effects of PV arrays on wind loads [22,23]. Other research groups have used wind tunnel tests, theoretical analysis, and numerical simulations to investigate the wind-induced vibration mechanism, aerodynamic instability, and impact of module tilt angles and geometric dimensions on wind vibration characteristics [24–28].

In recent years, with the development of PV power stations in mountainous regions and the intersection of agriculture, forestry, livestock, and fisheries, the terrain adaptability requirements for PV supports have become increasingly complex. To improve terrain adaptability, Baumgartner et al. proposed the cable-supported PV module system [29–31]. The cable-supported PV module system uses pre-tensioned cables to support PV modules, offering large spans, strong terrain adaptability, and cost-effectiveness. Since its development, the cable-supported PV module system has gained widespread attention in the PV industry. However, it experiences significant aerodynamic coupling effects and may cause severe component cracking or damage due to large wind-induced vibrations. There is limited research on cable-supported PV module systems, with the few published studies focusing on load values, wind-induced vibration characteristics, and vibration suppression measures.

Zhu et al. conducted fluid–structure interaction simulations to analyze the effects of cable pre-tension, tilt angle, and ground anchor cables on the wind vibration characteristics of cable-supported PV module systems [32,33]. Xu et al. and Li et al. used aeroelastic models and rigid models in wind tunnel tests to study the wind-induced vibrations of cable-supported PV module systems under different module tilt angles and cable pre-tension conditions [34]. Di et al. derived theoretical expressions for cable pre-tension and displacement in cable-supported PV module systems and analyzed their vibration characteristics [35]. Based on the findings of this study, Ding et al. used finite element simulations to analyze the failure modes of these systems [36]. He et al. used numerical simulations and wind tunnel tests to study the vibration characteristics of a 30-m span, DL cable-supported PV module system and proposed effective vibration suppression measures [37,38].

From the above analysis, it is clear that cable-supported PV module systems are ideal for PV power stations in complex terrain. However, research on their structural wind vibration safety remains insufficient. Specifically, research on the wind-induced vibration characteristics and the impact of inter-row interference effects is directly related to the optimization design and development of vibration suppression measures. Therefore, in the presented study, we used wind tunnel tests to analyze the wind vibration characteristics of a typical DL cable-supported PV module system, studied the shading effects of PV arrays, and explored the influence of wind direction and the initial tilt angles of PV modules on wind-induced vibration characteristics.

2. Wind Tunnel Test

2.1. Test Conditions

Wind tunnel tests were conducted at the Wind Tunnel Laboratory of Shijiazhuang Tiedao University. The experimental section of the wind tunnel comprises a width of 4.4 m, a height of 3.0 m, and a length of 24.0 m, with a wind speed range of 1.5 m/s to 30.0 m/s. The test model was placed on a turntable in the experimental section. To simulate the surface roughness characteristics according to the requirements of class B terrain, sharp edges and roughness elements were used in the incoming wind direction. As shown in Figure 1, the wind field uniformity in the central region of the test section was less than 0.5%, with a turbulence intensity of less than 1% and velocity instability of less than 0.6%. The wind tunnel's turntable has a diameter of 3 m, and the maximum length of the model is 3.4 m, which exceeds the diameter of the turntable. To accommodate this feature, aluminum alloy profiles were used to elevate and secure the tested model to the turntable, allowing for adjustment of the wind direction. To prevent damage to the wind field of the aluminum alloy profiles, wooden boards were laid over the profiles and extended to the entire wind tunnel test section, as shown in Figure 1.

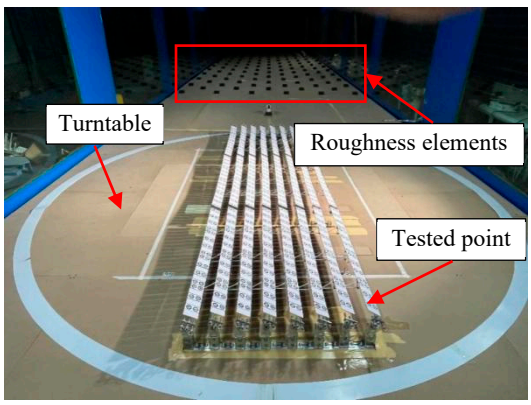

Figure 1. Wind tunnel test environment.

The main parameters tested in this experiment were the wind speed in the wind tunnel and the wind-induced displacement and torsional angle of the PV module. To measure the wind speed, two wind speed measurement probes were placed at the front of the first row of the PV array, on either side of the incoming wind direction, as shown in Figure 2. The height of the probes were the same as the PV modules. The probes used were the 3D pulsating wind speed measurement device, Series 100 Cobra, from Turbulent Flow Instrumentation, Australia. The accuracy of used probes is 0.1 m/s, as shown in Table 1. This device is capable of measuring instantaneous wind speed and static pressure, with a sampling frequency range of 0–2000 Hz and a wind speed measurement range of 2–100 m/s. The sampling frequency of probes were set to 70 Hz in this experiment. The tested wind speed and turbulence intensity profile tested in the wind tunnel were shown in Figure 3.

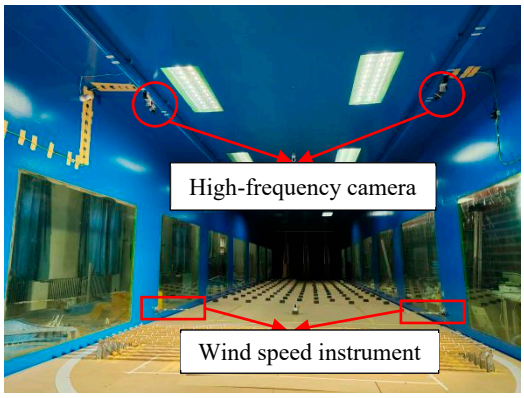

Figure 2. Installation of displacement and wind speed measuring instruments.

Table 1. Accuracy of the measuring devices.

Measuring Devices	Accuracy
Wind speed measurement probe	0.1 m/s
Three-dimensional displacement analyzer	0.01 mm

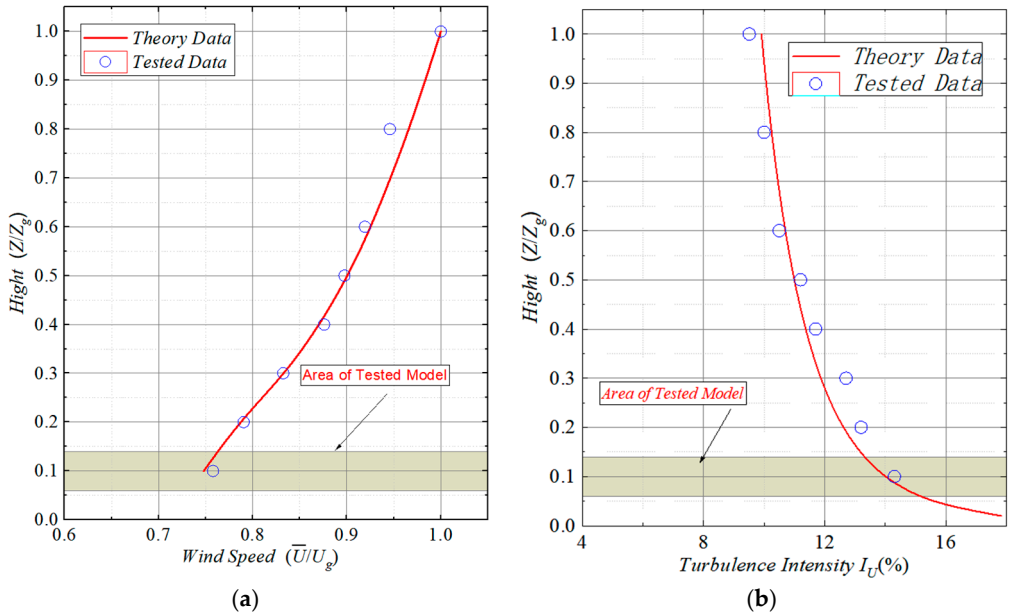

Figure 3. Wind speed and turbulence intensity profile tested in the wind tunnel: (**a**) wind speed profile; (**b**) turbulence intensity profile.

A three-dimensional displacement instrument was used to measure the displacement and rotational angle histories of the PV modules. The entire instrument includes an image acquisition system, test targets, and data analysis software. The image acquisition system uses two high-frequency cameras, which are fixed above the model using a magnetic base at the top of the wind tunnel, directly above the eighth row of the model, as shown in Figure 2. Stickers with marked tested points are attached to the surface of the PV modules that need to be measured. Each sticker has two tested points, and the displacement of the PV module is calculated based on the displacements of these two points. The accuracy of the three-dimensional displacement analyzer is 0.01 mm, as shown in Table 1, with a default sampling frequency of 243 Hz. For data storage considerations, the sampling frequencies for both wind speed and displacement were set to 70 Hz in this experiment.

2.2. Aeroelastic Model

The prototype studied in this paper is a typical DL cable-supported PV module system, as shown in Figure 4. In order to determine the wind vibration characteristics of the PV module system in different rows and spans, the model consists of eight rows, each with three spans, and each span is 34 m long. The inter-row spacing measures 4 m. Each row uses a dual-pillar form, and the two end pillars are fixed to the ground anchor pillars by diagonal cables. The average column height is 2.7 m, and the height is adjusted according to the tilt angle of the PV modules. The spacing between the upper cables is the same as the spacing between the PV module mounting holes, i.e., 1.4 m. The upper and lower cables comprise steel strand wires of different diameters, with the upper cables having a diameter of 15.2 mm and the lower cables having a diameter of 17.8 mm.

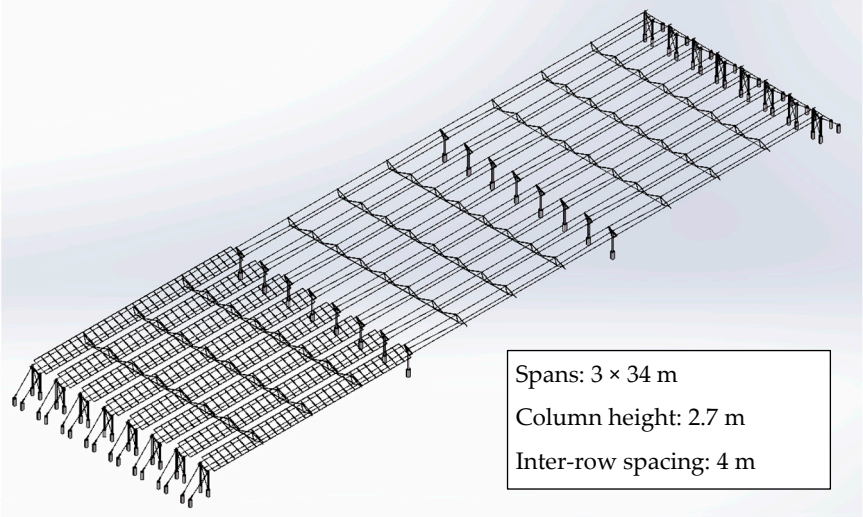

Figure 4. DL cable-supported PV module system.

The upper and lower cables are connected by triangular braces, with three braces installed at 1/4, 1/2, and 3/4 of the span. The triangular braces are isosceles triangles, with different heights based on their installation position. The triangular braces at the 1/2 position have a height of 0.8 m, while those at the 1/4 and 3/4 span positions have a height of 0.6 m. Lateral connections between rows are installed to enhance overall integrity. These lateral connections are located at the triangular braces and are rigidly connected through rigid rods. The dimensions of the PV modules are 2278 mm × 1134 mm × 30 mm, and the module weight is 35.65 kg. The gap between two adjacent PV modules measures 40 mm. The sag-span ratio is 1/100. The final natural frequency of the DL cable-supported PV module system is 0.96 Hz.

Based on the dimensions of the wind tunnel and total span of the prototype, the geometric scale ratio was determined to be 1:30. The materials selected for key components of the scaled model are presented in Table 2. Lightweight plywood was used to simulate the PV modules, and the mass of the panels was adjusted by attaching wallpaper to the back of the plywood. The plywood was connected to steel cables using AB glue. The vertical columns comprise profile steel, with no consideration given to their deformation. The original double-column structure with a connecting beam was simplified in the scaled model to a single column with a rotatable T-shaped steel plate beam structure, allowing the panel tilt angle to be easily adjusted. The steel cables were connected to the T-shaped steel plates at both ends using screws, with one end featuring a ring bolt for adjusting the pre-tension of the cables, thereby controlling the sag–span ratio.

Table 2. Materials for key components of the tested model.

	Key Components	Materials
1	PV module	76 mm × 38 mm × 2 mm plywood
2	Beam	T-shaped steel plate
3	Cable	0.4 mm diameter steel wire
4	Column	Steel
5	Row Interconnection and Triangular Brace	3D-printed nylon

The row interconnection and triangular bracing of the PV module system are made of 3D-printed nylon, ensuring both model accuracy and sufficient material strength and weight. When printing the triangular braces, small holes are left at the appropriate locations, through which the steel cables are connected to the braces. The triangular braces are attached to the plywood using lightweight glue, and the row interconnecting rods are fixed to the triangular braces with M4 bolts. Detailed assembly of the model is shown in Figure 5. The designed final natural frequency of the scaled model is 5.26 Hz.

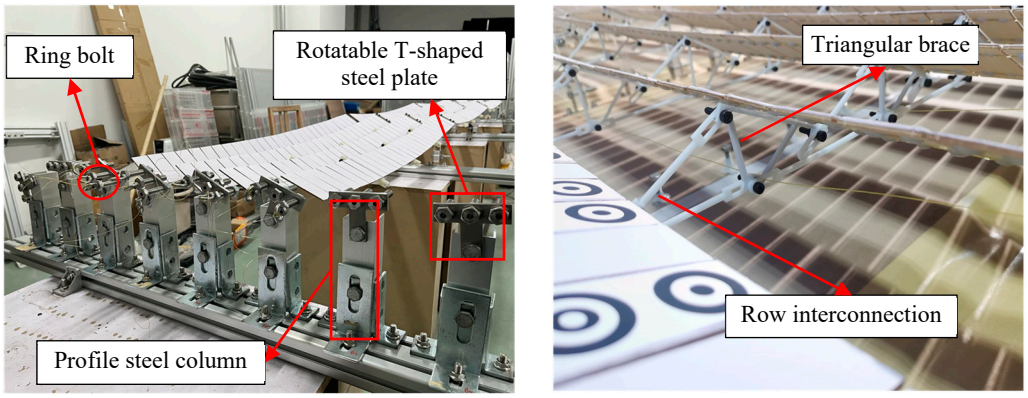

Figure 5. Detailed drawing of the tested model.

To verify the scaled model, the free decay method was used to test the fundamental natural frequency of the assembled aeroelastic model, which was found to be 5.23 Hz. The corresponding vibration mode was the vertical oscillation of the PV array. The measured fundamental natural frequency of the aeroelastic model was very close to the design value, indicating the validity of the model.

2.3. Parameter Definition

The main focus of this study is the vibration displacement and torsional angle of the PV modules. As shown in Figure 6, the angle between the PV module and the horizontal plane when stationary is defined as the initial design tilt angle of the module. When

the incoming wind direction is perpendicular to the cables and initially passes through the lower end of the PV module, the wind angle α is defined as 0°, which corresponds to the wind pressure condition. Conversely, when the wind direction is α = 180°, it corresponds to the wind suction condition. When the PV module undergoes vibration, it experiences both displacement vibration and torsional vibration. Displacement vibration is further divided into X-, Y-, and Z-direction vibrations. X-direction displacement refers to displacement parallel to the ground and parallel to the cable direction, Y-direction displacement refers to displacement parallel to the ground but perpendicular to the cable direction, and Z-direction displacement refers to vertical displacement perpendicular to the ground. The torsional angle θ refers to the rotational displacement of the PV module subjected to wind load. The symbols 'm' and 'd' represent the mean displacement and the standard deviation, respectively.

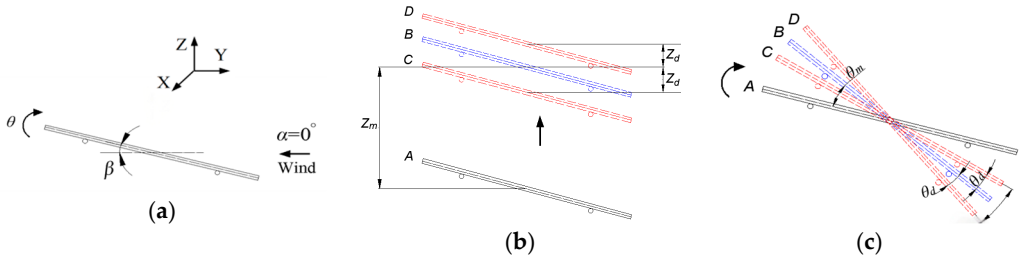

Figure 6. Illustration of PV module vibration: (**a**) schematic of different vibration directions; (**b**) schematic of vertical displacement vibration; (**c**) schematic of torsional vibration.

The displacement values are calculated by two tested points on each module surface, as described by Equations (1) and (2), where the displacement values are obtained through a three-dimensional displacement measurement instrument [37]. The displacement measurement instrument is capable of obtaining displacements and torsional angles with high precision, and the data collection rate is set to 70 Hz for both wind speed and displacement sampling.

$$Z_i = \frac{1}{2}(Z_{U,i} + Z_{D,i}) \tag{1}$$

$$\theta_i = \arcsin\left(\frac{Z_{U,i} - Z_{D,i}}{l}\right)\frac{180}{\pi} \tag{2}$$

where $Z_{U,i}$ and $Z_{D,i}$ denote the displacement of the upper and lower tested points of a certain PV module at the i-th sampling moment, respectively. Z_i denotes the displacement of a certain PV module at the i-th sampling moment, and θ_i denotes the torsional angle of a certain PV module at the i-th sampling moment. l denotes the distance between the centers of the two targets on the same PV module.

To determine the wind vibration characteristics of the PV module system under different wind directions and initial tilt angles, the wind direction angles selected for the experiment were 0°, 15°, 45°, 90°, 135°, 165°, and 180°. The initial tilt angles of the PV modules were 0°, 15°, and 25°. The wind speed ranged from 0 to 6 m/s, with a scaling factor of 1:30, and the corresponding actual wind speed was 0 to 32.9 m/s.

For the convenience of subsequent analysis, the PV array was numbered as shown in Figure 7. When the wind direction angle is 0°, the flow direction of the wind field for the first row is designated as R1, and subsequent rows are numbered sequentially up to R8. Each row is numbered from left to right, with the spans labeled as A, B, and C. A total of nine PV modules are tested in each row, numbered from left to right as module-1, 2, . . ., 9.

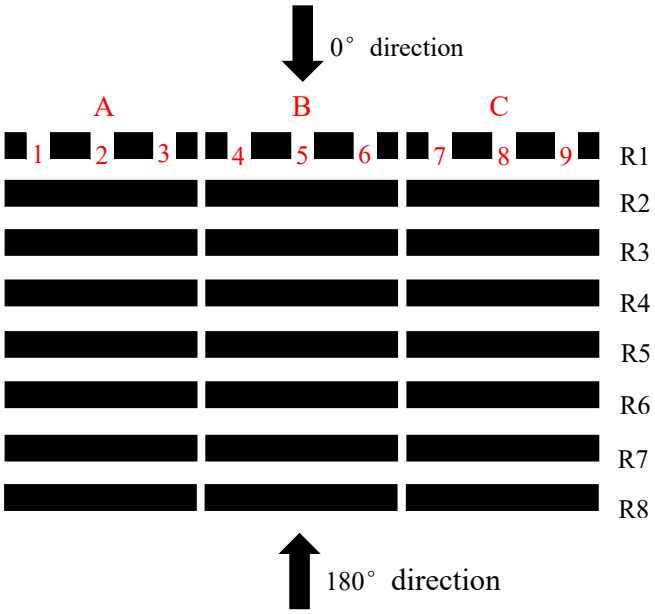

Figure 7. Schematic diagram of tested model numbering for the PV array.

3. Wind-Induced Vibration Characteristics Analysis

3.1. Displacement Analysis

In the wind tunnel test, a displacement measurement system based on image recognition technology was used, which allowed for the acquisition of displacement histories of PV modules in three coordinate directions. The displacement in three directions was compared and analyzed to identify the primary direction of wind-induced vibration for the DL cable-supported PV module system. Previous study results have shown that, for multi-row PV arrays, the first row of PV modules exhibits the largest wind-induced vibration [22,39,40]. The wind-induced displacement vibration of the PV modules was calculated using Equation (1). Figure 8 shows the displacement histories in three directions for the nine PV modules in the first row, R1, at a wind speed of 5.78 m/s.

From Figure 8, it can be seen that the displacement responses in the X, Y, and Z directions of the PV modules at different positions in R1 exhibit some fluctuating characteristics. Moreover, the displacement in the X–axis direction is almost zero, the displacement in the Y–axis direction is slightly greater than in the X–axis, but both X and Y directions are much smaller than the Z–axis direction. This indicates that the displacement response of the DL cable-supported PV module system is mainly in vertical vibration.

To further analyze the wind-induced displacement vibration of the PV module system at different wind speeds, Figure 9 shows the mean and standard deviation (STD) of displacement for three measurement points on the B-span in row R1, in the X, Y, and Z directions, as the wind speed increases. The wind speeds were 0.31, 3.45, 3.97, 4.63, 5.21, 5.79 m/s. As can be seen, the displacement in the X-direction does not change significantly with wind speed and remains close to zero. The displacement in the Y-direction shows a gradual increase as the wind speed rises. The displacement in the Z-direction is the largest for all PV modules at different wind speeds and exhibits a clearly nonlinear increase with wind speed. This finding further confirms that the displacement vibration of the PV module system primarily occurs in the vertical direction, and the difference between the vertical and the other two directions increases with wind speed.

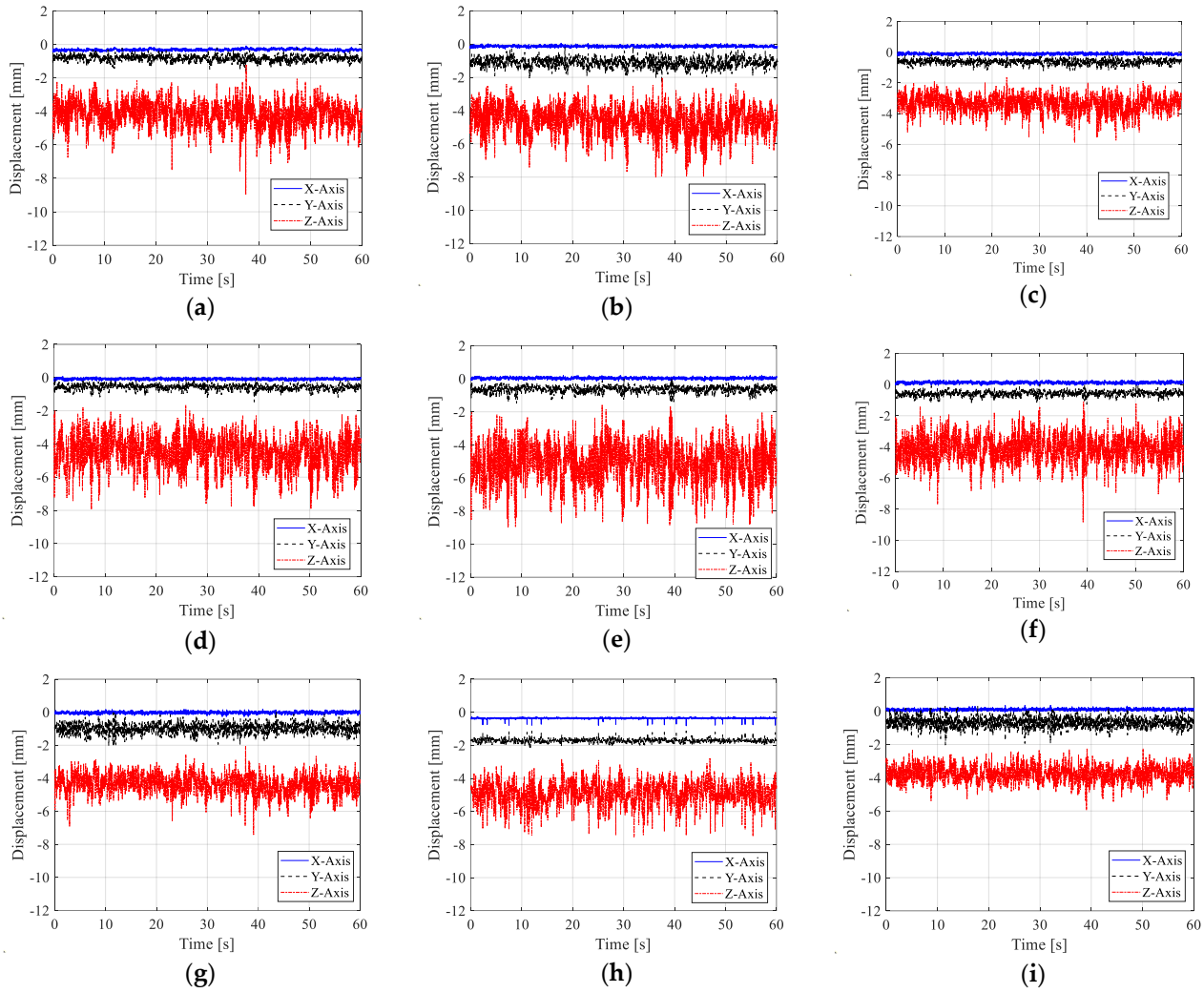

Figure 8. Histories of displacement responses in three directions for the PV modules in R1 at a wind speed of 5.78 m/s: (**a**) Module-1; (**b**) Module-2; (**c**) Module-3; (**d**) Module-4; (**e**) Module-5; (**f**) Module-6; (**g**) Module-7; (**h**) Module-8; (**i**) Module-9.

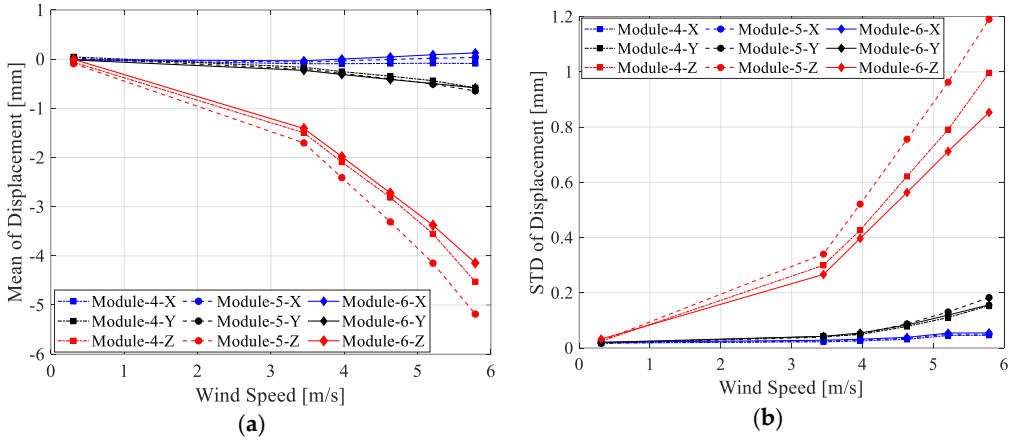

Figure 9. Variation in the mean and standard deviation (STD) of displacement with wind speed for PV modules in the middle B-span of the first row, R1: (**a**) mean of displacement variation with wind speed and (**b**) STD of displacement variation with wind speed.

Due to the shielding effect, the wind-induced vibration of the PV array in R1 is generally different from that in the subsequent rows. To investigate the inter-row shielding effect of the PV array, Figure 10 shows the distribution of wind-induced displacement vibration mean values and standard deviations for PV modules in the eight-row array.

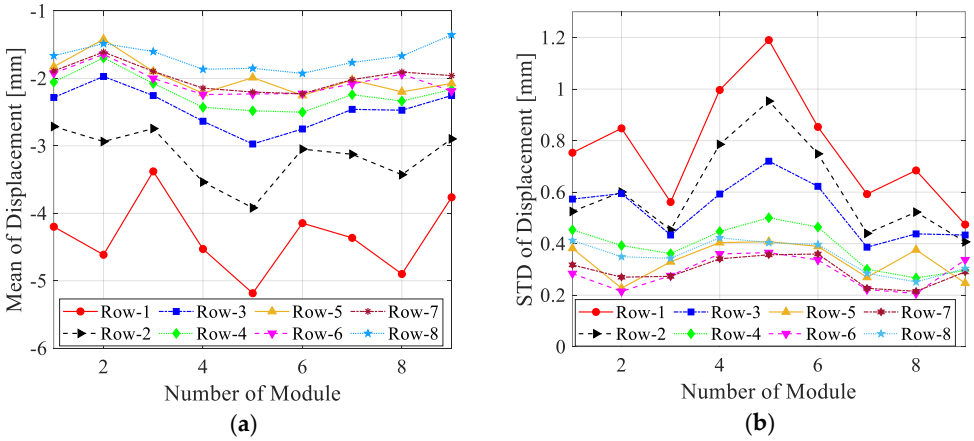

Figure 10. Mean value and standard deviation distribution of displacement for PV modules at different positions: (**a**) mean value distribution and (**b**) standard deviation distribution.

It can be seen that, whether for the mean value or standard deviation, the displacement response in R1 is larger than in the subsequent rows, indicating a significant shielding effect in the first row. Furthermore, it is clear that, for the first two rows of PV modules, the displacement response at the center of each span is greater than at the sides. For the later rows, the difference in wind-induced vibration response between the center and the sides decreases, indicating that the shielding effect reduces the difference in vibration response between different columns in the same row.

To provide a more detailed explanation of the wind-induced vibration of PV modules at different positions, Tables 3 and 4 present the mean values and standard deviations of displacement for different measurement points across various rows.

Table 3. Mean values of wind-induced vibration displacement.

Row	Module-1	Module-2	Module-3	Module-4	Module-5	Module-6	Module-7	Module-8	Module-9
1	−4.199	−4.614	−3.378	−4.529	−5.185	−4.146	−4.364	−4.900	−3.762
2	−2.713	−2.936	−2.744	−3.536	−3.919	−3.049	−3.125	−3.427	−2.896
3	−2.282	−1.971	−2.254	−2.635	−2.972	−2.749	−2.458	−2.472	−2.254
4	−2.054	−1.695	−2.075	−2.427	−2.480	−2.501	−2.241	−2.335	−2.164
5	−1.826	−1.419	−1.896	−2.220	−1.988	−2.252	−2.023	−2.199	−2.074
6	−1.924	−1.643	−2.000	−2.239	−2.230	−2.224	−2.082	−1.936	−2.188
7	−1.889	−1.609	−1.895	−2.14	−2.202	−2.227	−2.017	−1.905	−1.958
8	−1.663	−1.484	−1.601	−1.865	−1.850	−1.925	−1.764	−1.667	−1.354

Table 4. Standard deviations of wind-induced vibration displacement.

Row	Module-1	Module-2	Module-3	Module-4	Module-5	Module-6	Module-7	Module-8	Module-9
1	0.753	0.848	0.562	0.997	1.190	0.853	0.592	0.684	0.474
2	0.525	0.600	0.453	0.785	0.953	0.749	0.440	0.522	0.407
3	0.573	0.594	0.433	0.593	0.720	0.622	0.386	0.438	0.433
4	0.454	0.393	0.361	0.447	0.500	0.464	0.301	0.267	0.296
5	0.382	0.227	0.329	0.404	0.408	0.389	0.269	0.376	0.247
6	0.284	0.215	0.276	0.360	0.365	0.337	0.222	0.206	0.337
7	0.318	0.270	0.273	0.341	0.357	0.360	0.227	0.215	0.290
8	0.412	0.349	0.343	0.423	0.404	0.397	0.285	0.251	0.304

3.2. Wind-Induced Torsional Vibration Analysis

Due to the brittle nature of PV modules, torsional vibrations may pose a potential threat to their safety. To determine the wind-induced torsional vibration characteristics of the DL cable-supported PV modules, the wind-induced torsional vibration histories with a wind direction of 0°, initial tilt angle of 15°, and wind speed of 5.78 m/s were analyzed. Figure 11 shows the wind-induced torsional vibration histories for three tested PV modules at the center span, span-B, of the first row. As can be observed, the mean and STD of the torsional angle are very small, with mean values of −0.71°, −0.88°, and −0.58° and STD values of 0.19°, 0.21°, and 0.18° for Module-4, 5, and 6, respectively. Moreover, considering the PV module model dimensions of a length of 76 mm, the maximum mean value of 0.88° results in an edge displacement of less than 0.6 mm due to torsional vibrations. Compared to the vertical displacement of more than 5 mm for the same module, the torsional displacement is negligible.

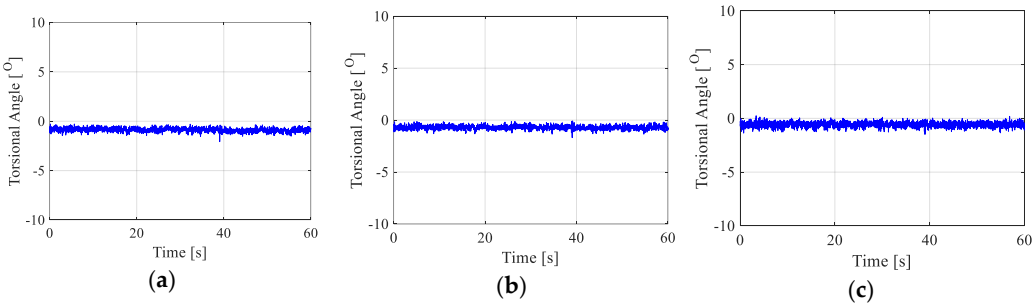

Figure 11. Wind-induced torsional angle histories for the three tested PV modules in the first row, span-A: (**a**) Module-4 torsional angle history; (**b**) Module-5 torsional angle history; (**c**) Module-6 torsional angle history.

To further analyze the torsional vibration of PV modules at different wind speeds, Figure 12 shows the mean and standard deviation of torsional angles of different tested modules in the first row as the wind speed changes. It can be seen that as the wind speed increases, neither the mean nor the standard deviation of the torsional angle shows any significant increase, with the torsional angle remaining close to zero.

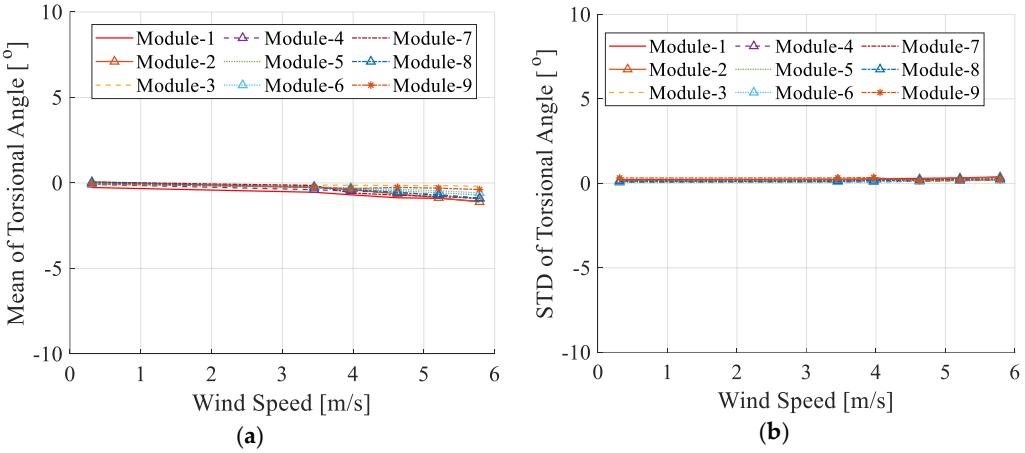

Figure 12. Mean and standard deviation of wind-induced torsional angles for PV modules at different wind speeds: (**a**) mean value and (**b**): standard deviation.

To explore the torsional vibration at different positions on the PV modules, Figure 13 shows the distribution of the mean and standard deviation of torsional angles of the different tested modules. It can be seen that the torsional angle mean and standard deviation

on the first row are larger, indicating that the first row still experiences a shielding effect. Additionally, it can be seen that, unlike displacement vibration, the torsional angles at different positions are relatively small.

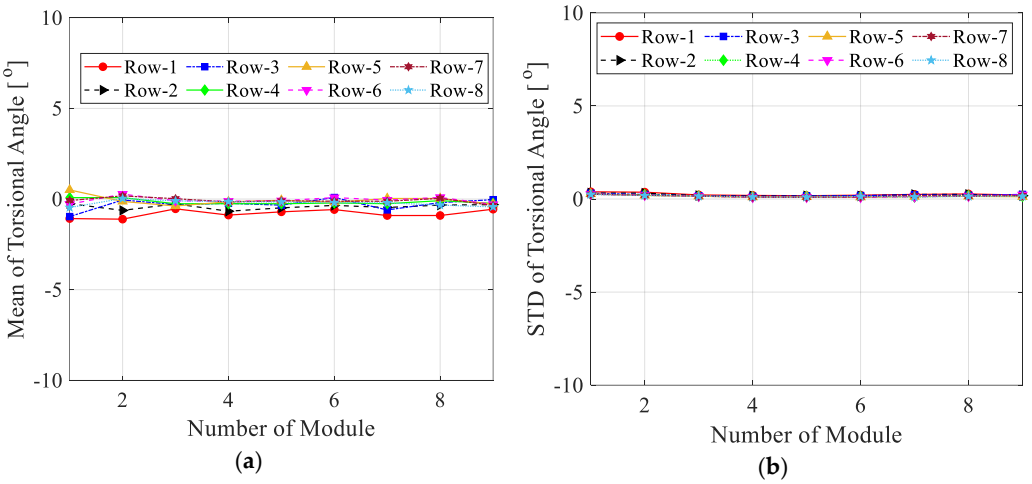

Figure 13. Mean value and standard deviation distribution of torsional angles for PV modules at different positions: (**a**) mean value distribution and (**b**) standard deviation distribution.

From the above analysis, it can be concluded that compared to the wind-induced displacement vibration of the PV module system, the torsional vibration is relatively small at different positions within the array and at different wind speeds. Therefore, for the wind-induced vibration response of the PV modules, the primary focus should be its displacement characteristics.

4. Influence of Wind Direction and Tilt Angle of PV Modules

PV power stations may be subject to wind loads from various directions during their service life, and wind loads from different direction angles can cause the wind-induced vibration characteristics of PV module systems to vary. Additionally, the incident angle of sunlight varies depending on the location of the PV power station, and PV module systems need to be designed with different initial tilt angles based on the incident angle of sunlight. Such changes lead to differences in the wind-induced vibration characteristics of PV module systems. To ensure the safety of DL cable-supported PV module systems under different initial module tilt angles and wind direction angles, it is crucial to first reveal the influence of these two factors on the wind-induced vibration characteristics. Therefore, tests were conducted under various initial PV module tilt angles and different wind direction angles.

4.1. Analysis of the Influence of Wind Direction Angle

Figure 14 shows the distribution of the mean and STD displacement values of the first row, R1, of PV modules under different wind direction angles, with a wind speed of 5.78 m/s. It can be observed that at wind direction angles of 0° and 180°, the displacement of the PV modules is greater than in other cases. Moreover, at 90° and 135°, the displacement responses are smaller than other cases. It was also observed that the wind-induced vibration at the 180° wind direction angle is greater than that at 0°, indicating that displacement vibrations are more significant under suction than under wind pressure. The explanation for this finding is the fact that the weight of the PV module creates pre-tension in the module, which provides significant stiffness against vertical displacement downwards. In contrast, vertical upward vibrations require the module to exceed a limit position before

stiffness is provided. Therefore, vertical upward vibrations caused by wind suction tend to be larger.

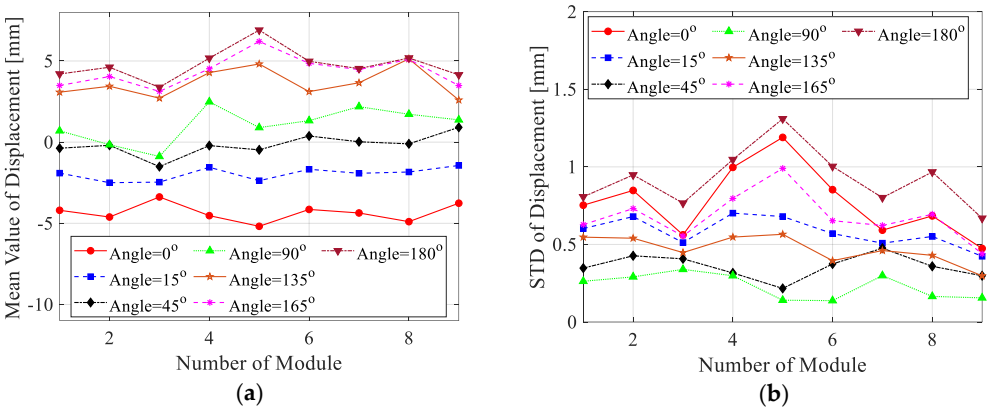

Figure 14. Distribution of the wind-induced displacement mean and STD values of R1: (**a**) distribution of mean displacement and (**b**) distribution of STD displacement.

In addition to affecting wind-induced displacement vibrations, the wind direction angle also influences the torsional vibrations of the PV modules. To further analyze the impact of different wind direction angles on the torsional vibrations of PV modules, Figure 15 shows the torsional vibration characteristics of the first row of PV modules under different wind direction angles. It can be seen that at a 180° wind direction angle, the torsional vibrations of the modules are most pronounced. Moreover, at different wind direction angles, the torsional vibrations of the PV modules are relatively small, and there is little variation in torsional vibration at different positions on the modules.

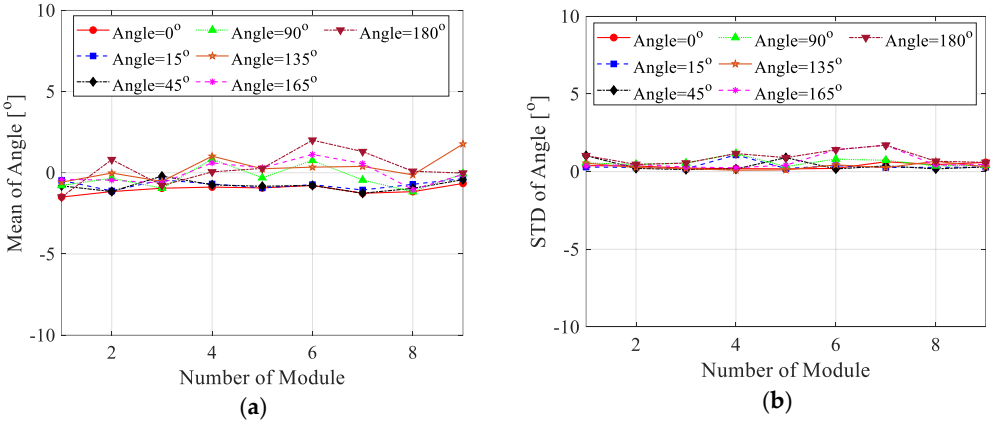

Figure 15. Distribution of wind-induced torsional angle mean and STD values of R1 under different wind direction angles: (**a**) mean values of torsional angle and (**b**) STD values of torsional angle.

4.2. Influence of Initial Tilt Angle

The initial tilt angle of PV modules affects the surrounding wind field, which, in turn, influences the wind loads acting on the modules, leading to changes in wind-induced vibration characteristics. To further analyze the impact of different initial PV module tilt angles on wind-induced vibration characteristics, Figure 16 shows the mean and STD values of the displacement vibrations of PV modules in the first row, R1, for initial tilt angles of 0°, 15°, and 25°, with a wind speed of 5.78 m/s and a wind direction angle of 0°. It can be seen that at an initial tilt angle of 25°, the mean and STD displacement values are the largest, and the response is most intense at the center of each span. This finding indicates that, within a limit range, the larger the tilt angle of the module, the larger the displacement vibrations.

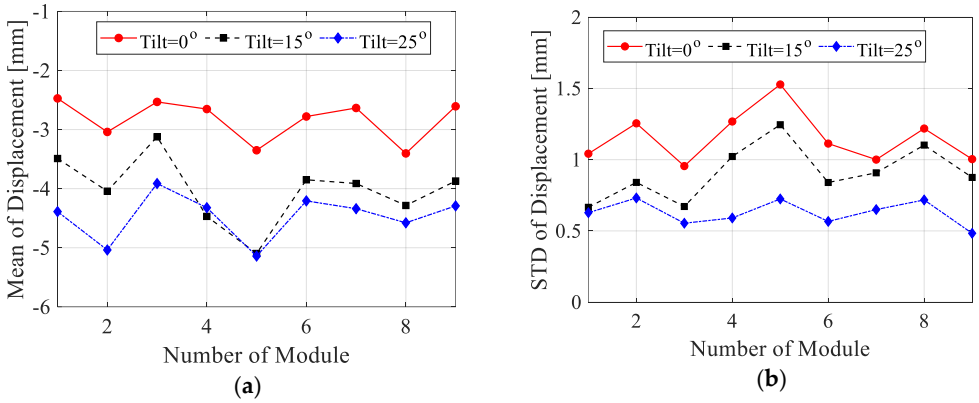

Figure 16. The mean and STD values of displacement for different PV modules in the first row: (**a**) mean values of displacement and (**b**) STD values of displacement.

To further analyze the impact of different initial tilt angles on the torsional vibrations of PV modules, Figure 17 presents the mean and STD values of the wind-induced torsional angles of PV modules in the first row at different positions, with a wind direction angle of 0° and a wind speed of 5.78 m/s. It can be seen that the wind-induced torsional angles are relatively small with the change in wind direction, with little variation. This finding further confirms that the primary wind-induced vibration response of DL cable-supported PV module systems is vertical displacement vibrations, and torsional vibrations can be neglected.

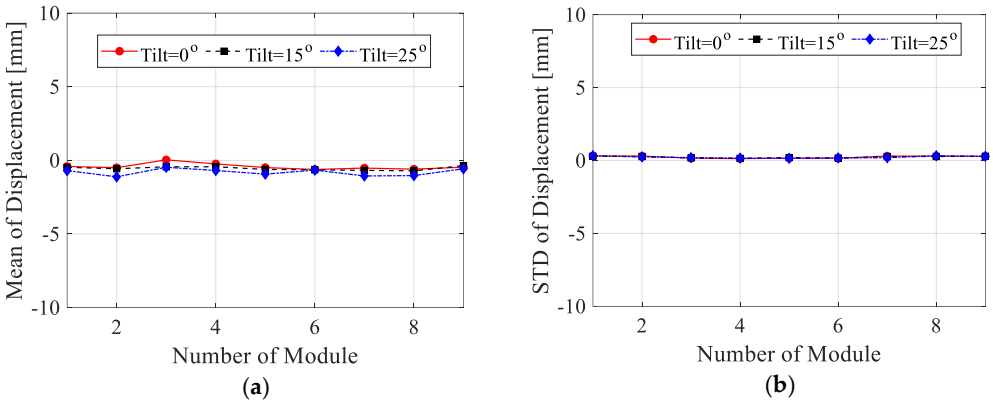

Figure 17. Mean and STD values of PV modules' torsional angles in the first row: (**a**) mean values of torsional angle and (**b**) STD values of torsional angle.

5. Conclusions

In this study, wind tunnel tests were conducted on a new type of DL cable-supported PV module system that has emerged in recent years. The test results revealed the wind-induced displacement and torsional vibration characteristics of the structure at different wind speeds. The shielding effect of the PV array was also studied, and the influences of different wind directions and the initial tilt angles of PV modules on the wind-induced vibration characteristics were analyzed. The following results were obtained:

(1) The vertical displacement vibrations of the DL cable-supported PV module system are the largest; in comparison, the displacement vibrations in other directions are much smaller. Wind-induced torsional vibrations are negligible compared to displacement vibrations.

(2) The wind-induced vibrations of the first row are significantly larger than those of the subsequent rows, indicating a clear shielding effect. In the same row, the response at the center span is greater than that at the sides.
(3) Wind direction angles of 0° and 180° cause the largest vibrations during wind pressure and wind suction, respectively, with the vibrations caused by wind suction being greater than those caused by wind pressure.
(4) Within a limit range, the larger the initial tilt angle of the PV module, the more pronounced the wind-induced vibrations.

6. Further Research and Limitations

In the vibration characteristics of DL cable-supported PV module system, the cable force is also the critical parameter. While, the cable was not tested in the wind tunnel test, and the characteristics of cable force was not studied. In the further research, the cable force of DL cable-supported PV module system will be studied. In addition, numerical simulation could offer a deeper understanding of the vibration characteristics under varying conditions, which will also be carried out in the following work.

Author Contributions: Conceptualization, Z.Z.; data curation, Z.X. and X.L.; formal analysis, Z.Z. and W.M.; funding acquisition, W.M.; investigation, Z.Z. and W.M.; writing—original, Z.Z. and Z.X.; writing—review and editing. All authors have read and agreed to the published version of the manuscript.

Funding: This research received no external funding.

Data Availability Statement: Data are contained within the article.

Acknowledgments: We are very grateful to Li Haiyun from Shijiazhuang Tiedao University for his instructive comments and great encouragement.

Conflicts of Interest: The authors declare no conflicts of interest.

References

1. Radu, A.; Axinte, E.; Theohari, C. Steady wind pressures on solar collectors on flatroofed buildings. *J. Wind. Eng. Ind. Aerodyn.* **1986**, *23*, 249–258. [CrossRef]
2. Li, J.Y.; Tong, L.W.; Wu, J.M.; Pan, Y.M. Numerical investigation of wind pressure coefficients for photovoltaic arrays mounted on building roofs. *KSCE J. Civ. Eng.* **2019**, *23*, 3606–3615. [CrossRef]
3. Peng, H.Y.; Dai, S.F.; Liu, H.J. Wind loading characteristics and roof zoning of solar arrays mounted on flat-roofed tall buildings. *J. Build. Eng.* **2023**, *66*, 105823. [CrossRef]
4. Estephan, J.; Chowdhury, A.G.; Irwin, P. A new experimental-numerical approach to estimate peak wind loads on roof-mounted photovoltaic systems by incorporating inflow turbulence and dynamic effects. *Eng. Struct.* **2021**, *252*, 113739. [CrossRef]
5. Wang, J.X.; Yang, Q.S.; Tamura, Y. Effects of building parameters on wind loads on flat-roof-mounted solar arrays. *J. Wind. Eng. Ind. Aerodyn.* **2018**, *174*, 210–224. [CrossRef]
6. Stenabaugh, S.E.; Iida, Y.; Kopp, G.A.; Karava, P. Wind loads on photovoltaic arrays mounted parallel to sloped roofs on low-rise buildings. *J. Wind. Eng. Ind. Aerodyn.* **2015**, *139*, 16–26. [CrossRef]
7. Wang, J.X.; Phuc, P.V.; Yang, Q.S.; Tamura, Y. LES study of wind pressure and flow characteristics of flat-roof-mounted solar arrays. *J. Wind. Eng. Ind. Aerodyn.* **2020**, *198*, 104096. [CrossRef]
8. Banks, D. The role of corner vortices in dictating peak wind loads on tilted flat solar panels mounted on large, flat roofs. *J. Wind. Eng. Ind. Aerodyn.* **2013**, *123*, 192–201. [CrossRef]
9. Wang, J.X.; Yang, Q.S.; Hui, Y. Comparisons of design wind pressures on roof-mounted solar arrays between wind tunnel tests and codes and standards. *Adv. Struct. Eng.* **2021**, *24*, 653–666. [CrossRef]
10. Dai, S.F.; Liu, H.J.; Peng, H.Y. Investigation into the effect of rounded building corner on wind loads of flat-roof-mounted solar arrays. *J. Build. Eng.* **2024**, *87*, 109048. [CrossRef]
11. Kopp, G.A.; Banks, D. Use of the Wind Tunnel Test Method for Obtaining Design Wind Loads on Roof-Mounted Solar Arrays. *J. Struct. Eng.* **2013**, *139*, 284–287. [CrossRef]

12. Naeiji, A.; Raji, F.; Zisis, I. Wind loads on residential scale rooftop photovoltaic panels. *J. Wind. Eng. Ind. Aerodyn.* **2017**, *168*, 228–246. [CrossRef]
13. Alrawashdeh, H.; Stathopoulos, T. Wind loads on solar panels mounted on flat roofs: Effect of geometric scale. *J. Wind. Eng. Ind. Aerodyn.* **2020**, *206*, 104339. [CrossRef]
14. Li, J.Y.; Tong, L.W.; Wu, J.M.; Pan, E.N. Numerical investigation of wind influences on photovoltaic arrays mounted on roof. *Eng. Appl. Comput. Fluid Mech.* **2019**, *13*, 905–922. [CrossRef]
15. Aly, A.M. On the evaluation of wind loads on solar panels: The scale issue. *Sol. Energy* **2016**, *135*, 423–434. [CrossRef]
16. Reina, G.P.; De Stefano, G. Computational evaluation of wind loads on sun-tracking ground-mounted photovoltaic panel arrays. *J. Wind. Eng. Ind. Aerodyn.* **2017**, *170*, 283–293. [CrossRef]
17. Sun, J.B.; He, Y.; Li, X.Y.; Lu, Z.; Yang, X.F. CFD simulations for layout optimal design for ground-mounted photovoltaic panel arrays. *J. Wind. Eng. Ind. Aerodyn.* **2023**, *242*, 105558. [CrossRef]
18. Agarwal, A.; Irtaza, H.; Ahmad, M.J. Numerical analysis of the ground-mounted solar PV panel array mounting systems subjected to basic wind for optimum design. *Can. J. Civ. Eng.* **2021**, *48*, 656–668. [CrossRef]
19. Aly, A.M.; Clarke, J. Wind design of solar panels for resilient and green communities: CFD with machine learning. *Sustain. Cities Soc.* **2023**, *94*, 104529. [CrossRef]
20. Wittwer, A.R.; Podesta, J.M.; Castro, H.G.; Mroginski, J.L.; Marighetti, J.O.; Bortoli, M.E.D.; Paz, R.R.; Mateo, F. Wind loading and its effects on photovoltaic modules: An experimental-Computational study to assess the stress on structures. *Sol. Energy* **2022**, *240*, 315–328. [CrossRef]
21. Eva, M.G.; Eduardo, B.M.; Jorge, P.G.; Antonio, N.M. Influence of inertia and aspect ratio on the torsional galloping of single-axis solar trackers. *Eng. Struct.* **2021**, *243*, 112682.
22. Ma, W.Y.; Zhang, W.D.; Zhang, X.B.; Chen, W.; Tan, Q. Experimental investigations on the wind load interference effects of single-axis solar tracker arrays. *Renew. Energy* **2023**, *202*, 566–580. [CrossRef]
23. Taylor, Z.J.; Browne, M.T.L. Hybrid pressure integration and buffeting analysis for multi-row wind loading in an array of single-axis trackers. *J. Wind. Eng. Ind. Aerodyn.* **2020**, *197*, 104056. [CrossRef]
24. Zhang, X.B.; Ma, W.Y.; Li, H.Y.; Shao, Q.J.; Kang, X.H. Experimental Investigation of the Torsional Aeroelastic Instability of Single-Axis Solar Trackers. *Int. J. Struct. Stab. Dyn.* **2023**, *24*, 2450007. [CrossRef]
25. Zhang, X.B.; Ma, W.Y.; Kang, X.H.; Shao, Q.J.; Tang, Z.Q. Experimental study of the torsional aeroelastic instability of single-axis solar trackers under different turbulence intensities. *J. Wind. Eng. Ind. Aerodyn.* **2023**, *240*, 105486. [CrossRef]
26. Taylor, Z.J.; Feero, M.A.; Browne, M.T.L. Aeroelastic instability mechanisms of single-axis solar trackers. *J. Wind. Eng. Ind. Aerodyn.* **2024**, *244*, 105626. [CrossRef]
27. Eva, M.G.; Eduardo, B.M.; Jorge, G.P.; Antonio, N.M. Experimental determination of the resistance of a single-axis solar tracker to torsional galloping. *Struct. Eng. Mech.* **2021**, *78*, 519–528.
28. Valentin, D.; Valero, C.; Egusquiza, M.; Presas, A. Failure investigation of a solar tracker due to wind-induced torsional galloping. *Eng. Fail. Anal.* **2022**, *135*, 106137. [CrossRef]
29. Baumgartner, F.P.; Büchel, A.; Bartholet, R. Solar wings: A new lightweight photovoltaic tracking system. In Proceedings of the 23rd European Photovoltaic Solar Energy Conference, Valencia, Spain, 1–5 September 2008.
30. Baumgartner, F.P.; Büchel, A.; Bartholet, R. Experiences with cable-based solar wings tracking system and progress towards two axis large scale solar systems. In Proceedings of the 24th European Photovoltaic Solar Energy Conference, Hamburg, Germany, 21–24 September 2009.
31. Baumgartner, F.P.; Büchel, A.; Bartholet, R. Cable-based solar wings tracking system: Two-axis system and progress of one-axis system. In Proceedings of the 25th European Photovoltaic Solar Energy Conference, Valencia, Spain, 6–9 September 2010.
32. Zhu, Y.F.; Huang, Y.; Xu, C.Z.; Xiao, B.; Chen, C.H.; Yao, Y. Analysis of wind-induced vibration effect parameters in flexible cable-supported photovoltaic systems: A case study on ground anchor with steel cables. *Case Stud. Constr. Mater.* **2024**, *20*, e03368. [CrossRef]
33. Zhu, Y.F.; Huang, Y.; Xu, C.Z.; Xiao, B.; Chen, C.H.; Yao, Y. Effect of tilt angle on wind-induced vibration in pre-stressed flexible cable-supported photovoltaic systems. *Sol. Energy* **2024**, *277*, 112729. [CrossRef]
34. Xu, H.W.; Ding, K.Y.; Shen, G.H.; Du, H.; Chen, Y. Experimental investigation on wind-induced vibration of photovoltaic modules supported by suspension cables. *Eng. Struct.* **2024**, *299*, 117125. [CrossRef]
35. Di, Z.H.; Wang, F.; Yu, H.L.; Dai, X.; Luo, B.; Liu, X. Analytical formulation and optimization of the initial morphology of double-Layer cable truss flexible photovoltaic supports. *Buildings* **2024**, *14*, 2549. [CrossRef]
36. Ding, H.; He, X.H.; Jing, H.Q.; Wu, X.P.; Weng, X.J. Design method of primary structures of a cost-effective cable-supported photovoltaic system. *Appl. Sci.* **2023**, *13*, 2968. [CrossRef]
37. He, X.H.; Ding, H.; Jing, H.Q.; Wu, X.P.; Weng, X.J. Mechanical characteristics of a new type of cable-supported photovoltaic module system. *Sol. Energy* **2021**, *226*, 408–420. [CrossRef]

38. He, X.H.; Ding, H.; Jing, H.Q.; Zhang, F.; Wu, X.P.; Weng, X.J. Wind-induced vibration and its suppression of photovoltaic modules supported by suspension cables. *J. Wind. Eng. Ind. Aerodyn.* **2020**, *206*, 104275. [CrossRef]
39. Li, J.L.; Hong, G.H.; Xu, H.W. Wind Load Effects and Gust Loading Factor for Cable-Suspended Photovoltaic Structures. *Energies* **2024**, *17*, 38. [CrossRef]
40. Zhang, X.B.; Ma, W.Y.; Zhang, Z.K.; Hu, L.; Cui, Y.Y. Experimental study on the interference effect of the wind-induced large torsional vibration of single-axis solar tracker arrays. *J. Wind. Eng. Ind. Aerodyn.* **2023**, *240*, 105470. [CrossRef]